Dopant activation in Sn-doped Ga2O3 investigated by X-ray absorption spectroscopy

Dopant activation in Sn-doped Ga_2O_3 investigated by X-ray absorption spectroscopy

S. C. Siah,[1,a)], R. E. Brandt[1], K. Lim[2,3], L. T. Schelhas[2], R. Jaramillo[1], M. D. Heinemann[4], D. Chua[5], J. Wright[6], J. D. Perkins[7], C. U. Segre[6], R. G. Gordon[5], M. F. Toney[2], T. Buonassisi[1,b)]

[1]*Massachusetts Institute of Technology, Cambridge, Massachusetts, 02139, USA*

[2]*SLAC National Accelerator Laboratory, Stanford Synchrotron Radiation Laboratory Lightsource, Menlo Park, California, 94025, USA*

[3]*Department of Materials Science and Engineering, Stanford University, Stanford, California, 94305, USA*

[4]*PVcomB, Helmholtz-Zentrum Berlin, 12489 Berlin, Germany*

[5]*Department of Chemistry Materials Science and Chemical Biology, Harvard University, Cambridge, Massachusetts, 02138, USA*

[6]*Physics Department and CSRRI, Illinois Institute of Technology, Chicago, Illinois 606016, USA*

[7]*National Renewable Energy Laboratory, Golden, Colorado 80401, USA*

[a)] Electronic mail: sincheng@alum.mit.edu

[b)] Electronic mail: buonassisi@mit.edu

Abstract

Doping activity in both beta-phase (β-) and amorphous (a-) Sn-doped gallium oxide (Ga_2O_3:Sn) is investigated by X-ray absorption spectroscopy (XAS). A single crystal of β-Ga_2O_3:Sn grown using edge-defined film-fed growth at 1725 °C is compared with amorphous Ga_2O_3:Sn films deposited at low temperature (<300 °C). Our XAS analyses indicate that activated Sn dopant atoms in conductive single crystal β-Ga_2O_3:Sn are present as Sn^{4+}, preferentially substituting for Ga at the octahedral site, as predicted by theoretical calculations. In contrast, inactive Sn atoms in resistive a-Ga_2O_3:Sn are present in either +2 or +4 charge states depending on growth conditions. These observations suggest the importance of growing Ga_2O_3:Sn at high temperature to obtain a crystalline phase and controlling the oxidation state of Sn during growth to achieve dopant activation.

Many optoelectronic devices incorporate a transparent conducting oxide (TCO) to transport charge carriers and photons to and from active semiconductor layers. An outstanding materials challenge is to develop a wide-bandgap TCO with both small electron affinity and high donor concentration (Fermi energy), enabling a low-loss electron-selective contact for emerging materials with high conduction-band energies including GaN, Cu_2O, and *n*-type silicon.

For this purpose, beta-phase gallium oxide (β-Ga_2O_3) has recently emerged as a promising candidate TCO. With an electron affinity of 3.7 eV,[1] bandgap of 4.8 eV[2] and transmissivity above 80% in the wavelength range of 300 to 1000 nm,[3] Ga_2O_3 appears to be an excellent candidate wide-bandgap TCO with low electron affinity. Ga_2O_3 can be doped with tin, achieving donor concentrations above 10^{19} cm^{-3} when grown in bulk-crystal form[3] and above 10^{18} cm^{-3} when deposited by molecular-beam epitaxy (MBE) in the 540 to 600°C range.[4] However, thin films deposited using atomic-layer deposition (ALD) and pulsed-laser deposition (PLD) at more moderate temperatures in the 100 to 200°C range have not exhibited high Sn dopant activation; as observed in this work, these films are typically highly resistive, even with a concentration of 10^{20} cm^{-3} Sn dopants. Identifying a means to achieve higher Sn dopant activation in low-temperature ALD- or PLD- deposited films could increase the industrial relevance of Ga_2O_3:Sn for cost-sensitive applications including field-effect transistors,[4] solar cells,[5–7] gas sensors,[8] and lasers.[9] Determining the chemical states of active and inactive Sn dopants in Ga_2O_3 is a first and necessary step toward developing intuition and theory to guide thin-film synthesis.

Herein, the chemical state of Sn dopants in β-Ga_2O_3 bulk crystals and amorphous (a-) Ga_2O_3 thin films deposited by ALD and PLD is investigated. Synchrotron-based X-ray absorption spectroscopy (XAS), a probe of local atomic structure and chemical state, is employed to define requirements for successful dopant activation. It is found that Sn dopant activation correlates

with Sn chemical state and Ga_2O_3 matrix crystallinity. The local structures of the metal cations in these different samples provide insights into how dopant atoms are incorporated into the host Ga_2O_3 lattices and govern electrical conductivity.

β-Ga_2O_3:Sn single crystal (SC) is purchased commercially from Tamura Corporation and is grown from the melt using the edge-defined film-fed growth (EFG) method.[4] In addition, a-Ga_2O_3:Sn thin films are deposited using ALD and PLD methods. The ALD film is deposited at 120 °C in a custom-built cylindrical reactor with a 30 cm long and 3 cm wide sample stage, and a chamber volume of 0.627 L. The Ga and Sn precursors used in the ALD process are bis(μ-dimethylamino)tetrakis(dimethylamino)digallium[6,10] and tetrakis(dimethylamido)tin(IV) respectively. The oxygen source is H_2O. During the ALD process, the temperatures of the Ga and Sn precursors are maintained at 120 and 60 °C, respectively, while H_2O is kept at 25 °C. High-purity N_2 is used as a carrier gas and the dose pressure of the gallium precursor and H_2O are estimated to be approximately 3 and 5 Torr s, respectively. The Ga_2O_3:Sn films are deposited on Si/SiO_2 substrate by repeating a supercycle consisting of 19-times subcycle of Ga_2O_3 (bis(μ-dimethylamino)tetrakis(dimethylamino)digallium/purge/H_2O/purge) followed by 1 time subcycle of SnO_2 (tetrakis(dimethylamido)tin(IV)/purge/ H_2O/purge). Purge time is set to be 30 s. The deposition rate is measured to be ~0.2 nm per subcycle. The PLD film is deposited on quartz substrate using Ga_2O_3 and SnO_2 targets and the energy density of the pulsed KrF excimer laser (248 nm) is set to 300 mJ with a repetition rate of 10 Hz and a distance of 10 cm between the target and the sample substrate. The substrate is rotated during the 50 laser pulses applied to the Ga_2O_3 target, and kept at a fixed angle during 2 pulses applied to the SnO_2 target. This procedure is repeated 400 times, resulting in a homogeneous Ga_2O_3 film with a Sn doping gradient across the sample from approximately 1 at.% to 4 at.%. The oxygen partial pressure is set to 100 μTorr

for the depositions at 400°C to ensure that the film is close to stoichiometric. The thickness of both the ALD and PLD films are about 200 nm and no post annealing is performed for both ALD and PLD samples.

The stoichiometry of the ALD and PLD thin films are measured using Rutherford Backscattering Spectroscopy (RBS) and determined to be $Ga_2O_{3.41}Sn_{0.065}$ and $Ga_2O_{2.91}Sn_{0.072}$ respectively. Accordingly, the atomic wt. % of Sn for ALD and PLD thin films are estimated to be 2.3×10^{20} and 2.9×10^{20} cm^{-3} respectively. The atomic wt. % of Sn for a set of SC samples are obtained from Tamura Corporation for comparison. In addition, the net carrier density for SC Ga_2O_3:Sn samples determined by electrochemical capacitance-voltage (ECV) are also obtained from Tamura Corporation. Hall and four-point probe measurements are performed for all the samples using a Ga_2O_3:Sn/Ti (100 nm)/Au (100 nm) stack for ohmic contact[11] but only the SC Ga_2O_3:Sn sample exhibits detectable signals. The Hall mobility and net carrier density (N_D-N_A) of the SC are determined to be 110 $cm^2/V\cdot s$ and $4\times\times10^{18}$ cm^{-3} (N_D-N_A by ECV = $7\times\times10^{18}$ cm^{-3}) respectively. The ALD and PLD film structures were also analyzed with wide angle X-ray diffraction (XRD) on Beamline 11-3 at the Stanford Synchrotron Radiation Lightsource (SSRL). Two-dimensional scattering was collected with a MAR345 image plate at grazing incidence at an incident energy of 12.7 keV. Spectra were integrated between $5^o < \phi < 175^o$ using the GSAS II analysis software. The resistivities for our ALD and PLD samples are estimated to be > 2000 Ω cm based on the detection limit of the four-point probe system. By assuming a mobility of > 0.1 cm^2/V s, the upper limit of carrier density is estimated to be 3.0×10^{16} cm^{-3} for our a-Ga_2O_3:Sn films. Figure 5 compares the net carrier density of all experimental samples as a function of Sn concentration, including data obtained from Tamura Corporation for a suite of SC samples with different Sn concentrations. The SC samples grown via EFG have an activation ratio close to

100%, whereas the Sn dopant atoms in our ALD and PLD deposited films are either largely un-activated or highly compensated, as evident through their high resistivities and low carrier concentrations.

We perform Ga *K*-edge XAS at Beamline 4-3 of the Stanford Synchrotron Radiation Lightsource and Sn *K*-edge XAS at MRCAT Beamline 10-ID of the Advanced Photon Source. In both measurements, the thin-film samples are measured in fluorescence mode with an incident beam of approximately 500 × 500 μm^2. The *K*-edge fluorescence for Ga and Sn is measured by a Lytle detector and silicon Vortex solid-state detector respectively. Reference metallic Ga or Sn thin-foils are measured to account for relative energy drifts. The X-ray absorption near-edge structures (XANES) and extended X-ray absorption fine structures (EXAFS) are isolated by normalizing the absorption spectrum and subtracting the smooth atomic background absorption signal from the measured absorption signal using the AUTOBK algorithm in Athena with R_{bkg} = 1.0 Å.[12–14] After background removal, the processed data are transformed from energy space to k-space using the relationship, $k^2 = 2m(E - E_0)/\hbar^2$, where k is the electron wavenumber, m is the electron mass, E_0 is the *K*-edge absorption energy of the respective elements, and $\hbar$ is Planck's constant. The spectra are weighted by k^2 to compensate for amplitude decay. For further analysis, the k^2-weighted spectra data are Fourier-transformed with a Hanning window as a bandpass filter to enhance the signal to noise ratio within windows between k = 1.5 to 10.0 Å^{-1}.

The chemical states of Sn for each sample can be derived by comparing, in Figure 6, the respective XANES spectra with Sn metal foil, SnO powder and SnO_2 powder references. The full XANES spectra is given in Figure S.1.[15] The relative chemical shifts observed in the XANES spectra are due to changes in oxidation state, which alters the binding energy for electrons in the first shell.[16] Figure 6 shows that the average charge states of Sn atoms in our SC

and ALD samples are similar to that of SnO_2 (Sn^{4+}). Comparing this with the resistivity data suggests that Sn^{4+} can function as an electron donor under the correct conditions. However, its presence does not always result in free electrons due to other reasons including the formation of compensating defects or formation of secondary phases. The average oxidation state in our PLD sample corresponds to Sn^{2+} (SnO) which is not likely to act as an electron donor. The presence of this reduced state (compared to the SC and ALD) suggests that the growth environment could be too reducing relative to the ALD and SC growth processes.

Next, EXAFS is used to investigate the structural origin of Sn doping. Figure 7 shows the Fourier-transformed spectra plotted as the magnitude, $|\chi(R)|$, for both the Ga and Sn *K*-edges. The first large peak in the $|\chi(R)|$ spectrum is due to only single-scattering paths from the first nearest neighbor (1NN) shell of atoms, and higher-order peaks are due to single- and multiple-scattering paths involving neighboring atoms in 1NN and higher order shells. In both sets of spectra, the amplitudes of $|\chi(R)|$ from higher-order shells (R > 2 Å) for the ALD and PLD deposited samples are strongly attenuated, showing limited structural order beyond 1NN. The lack of long-range order is consistent with the amorphous structure as characterized by our XRD measurements as shown in supplemental Figure S.2.[17]

To gain quantitative local structural information, the peaks are isolated and fitted using the EXAFS equation given by:[18]

$$\chi(k) = S_0^2 \sum_j \frac{N_j f_j(k)}{kR_j^2} e^{-2k^2\sigma_j^2} e^{-2R_j/\lambda(k)} \sin(2kR_j + \delta_j(k)), \quad (1)$$

where j indicates shells of like atoms, S_0^2 is the passive electron reduction factor, N_j is the coordination number of atoms in the j^{th} shell, k is the photoelectron wavenumber, R_j is the half

path length, σ_j^2 is the Debye-Waller factor or the mean-squared disorder of neighbor distance and $\lambda(k)$ is the electron mean free path. The scattering amplitude, $f_j(k)$, and the phase shift, $\delta_j(k)$, are dependent on the atomic number of the scattering atoms. S_0^2 for both Ga (1.00) and Sn (1.14) are determined by fitting the crystalline Ga_2O_3:Sn SC sample and used as constants for other samples. The other fitting parameters for each scattering path are the changes in the half path length (ΔR_{eff}), σ_j^2 and energy shift (ΔE_0). For the SC sample, the spectra is fitted up to the second-order peak, and the scattering paths used in the data fitting routines are calculated using the crystal structure of β-Ga_2O_3:Sn (space group C12/m1)[19,20] as a starting input into the ATOMS and FEFF6 codes implemented in Artemis.[21] In the unit cell of β-Ga_2O_3, there are two crystallographically nonequivalent Ga atoms (tetrahedral Ga1 and octahedral Ga2) and three nonequivalent O atoms (O1, O2 and O3). The Ga *K*-edge spectrum for the SC sample is modeled by considering equal contributions from the Ga1 and Ga2 sites,[22] and the Sn *K*-edge spectrum is fitted by considering either substitutional Sn-on-Ga1 (Sn_{Ga1}) or Sn-on-Ga2 (Sn_{Ga2}) defects. Scattering path-lengths up to 3.5 Å are considered for fitting the SC sample. For the amorphous thin-film samples, only the first-order peak is fitted by considering Ga–O and Sn–O bonds in the 1NN shell. The non-linear least squares fitting routine is subsequently performed in Artemis to obtain the best-fit parameters. The best-fit parameters for the Sn *K*-edge spectra are included in Table II, while those for the Ga *K*-edge spectra are included as supplemental materials in Table S.I[23] as many scattering paths are involved. Both $|\chi(R)|$ and k^2-weighted $|\chi(k)|$ spectra are shown in Figure 7 and 4 respectively. However, both the real and imaginary parts of $\chi(R)$ are included as supplemental materials in Figure S.3[24] and Figure S.4.[25]

As shown in Figure 7(a) and 4(a), the good agreement between the Ga *K*-edge spectrum for the SC β-Ga_2O_3:Sn and our model up to the second order shell corroborates the beta-phase nature of the host lattice as determined using XRD by other authors.[26] By considering two different possibilities in which Sn atoms can be incorporated into the SC β-Ga_2O_3 host lattice, it is observed that there is a preferential substitution at the Ga2 octahedral site (Sn_{Ga2}, *R*-factor = 0.01) as compared to substitution at the Ga1 (Sn_{Ga1}, *R*-factor = 0.05). Our observation is also consistent with first-principles calculations by Varley *et al.*[27] Several other studies have also shown that transition metals like In,[28] Cr,[29] and Mn[30] have a preference for the octahedral site and can be explained by steric reasons.[29,30]

For the ALD and PLD amorphous thin-films, the average coordination number to O atoms in Sn's 1NN shell is found to be close to 5.0, despite the difference in charge state of the central absorbing Sn atoms. This suggests that our amorphous films might not be deposited in thermodynamic equilibrium conditions, because Sn atoms in SnO_2 (Sn^{4+}) and SnO (Sn^{2+}) tend to favor octahedral and tetrahedral coordination respectively. Despite similar coordination numbers, the larger Sn^{2+} ions in the PLD thin-film increases the average Sn–O bond-length (R_{eff} = 2.117 Å) as well as the structural disorder (σ^2 = 0.0128 $Å^{-2}$) relative to the ALD films (R_{eff} = 2.030 Å and σ^2 = 0.0076 $Å^{-2}$). The lack of long range order in both ALD and PLD thin-films suggests that a non-crystalline structure could represent an impediment for dopant activation. One further explanation for the ALD thin-film to exhibit low conductivity despite the presence of Sn^{4+} could be the formation of a compensating defect in the that reduces the number of "activated" Sn^{4+}; such phenomenon has been observed in crystalline ZnO:Ga.[31] Lastly, post-annealing has been performed in this work in an attempt to activate the dopants in ALD Ga_2O_3:Sn thin-films (1 hour in N_2 atmosphere at 1000ºC). However, both the film resistivity and crystalline order did not

exhibit any detectable change and the authors are of the opinion that it might be necessary to anneal the films beyond 1000ºC to achieve crystalline Ga_2O_3 for dopant activation.

In conclusion, XAS is used to investigate the differences in the local structures of conductive single-crystal β-Ga_2O_3:Sn and resistive a-Ga_2O_3:Sn thin-films. Our results can be used to help engineer Ga_2O_3:Sn thin-films with the favorable electrical properties of single crystal β-Ga_2O_3:Sn. Our XAS analyses indicate that activated Sn dopant atoms in conductive single-crystal β-Ga_2O_3:Sn are present as Sn^{4+}, which preferentially substitutes for Ga at the octahedral Ga2 site as predicted by previous theoretical calculations. On the other hand, inactive Sn dopants in resistive a-Ga_2O_3 are present in either +2 or +4 charge states, depending on growth conditions. Lastly, XAS results indicate a lack of structural order beyond the 1NN shell in a-Ga_2O_3 samples, which might suggests that a crystalline structure might be necessary for high dopant activation. Consequently, achieving crystalline Ga_2O_3 and controlling the oxidation state of Sn during growth are both both appear to be necessary to obtain high Ga_2O_3 conductivity.

This work is supported as part of the Center for Next Generation Materials by Design (CMGMD), an Energy Frontier Research Center funded by the U.S. Department of Energy, Office of Science, Basic Energy Sciences under Contract No. DE-AC36-08GO28308. Use of the Stanford Synchrotron Radiation Lightsource, SLAC National Accelerator Laboratory, is supported by the U.S. Department of Energy, Office of Basic Energy Sciences under Contract No. DE-AC02-76SF00515. Use of the Advanced Photon Source at Argonne National Laboratory is supported by the U. S. Department of Energy, Office of Science, Office of Basic Energy Sciences, under Contract No. DE-AC02-06CH11357. MRCAT operations are supported by the Department of Energy and the MRCAT member institutions. S. Lany, D.S. Ginley, W. Tumas (NREL) and A.M. Kolpak (MIT) are thanked for helpful discussions. S.C.S., R.E.B., K.L and

R.J acknowledge a Clean Energy Scholarship from NRF Singapore, an NSF Graduate Research Fellowship, a Kwanjeong Education Foundation Fellowship and a U. S. Department of Energy EERE Postdoctoral Research Award, respectively. Lastly, Tamura Corporation is thanked for providing insightful information.

S.C.S., R.E.B., R.J., & T.B. designed the experiment; M.D.H. & D.C. fabricated the PLD and ALD samples, respectively; S.C.S. performed Hall; J.D.P performed RBS; L.S. performed XRD at SLAC; S.C.S., R.E.B., R.J., T.B., L.S., K.L., J.W. & C.U.S. acquired XAS data; S.C.S. fitted the XAS data; S.C.S. wrote the paper; R.G.G., M.T., & T.B. supervised the research. All authors reviewed and commented on the manuscript.

[1] T.S. Lay, M. Hong, J. Kwo, J.P. Mannaerts, W.H. Hung, and D.J. Huang, Solid. State. Electron. **45**, 1679 (2001).

[2] E.G. Víllora, K. Shimamura, Y. Yoshikawa, T. Ujiie, and K. Aoki, Appl. Phys. Lett. **92**, 202120 (2008).

[3] N. Suzuki, S. Ohira, M. Tanaka, T. Sugawara, K. Nakajima, and T. Shishido, Phys. Status Solidi Curr. Top. Solid State Phys. **4**, 2310 (2007).

[4] M. Higashiwaki, K. Sasaki, A. Kuramata, T. Masui, and S. Yamakoshi, Phys. Status Solidi Appl. Mater. Sci. **211**, 21 (2014).

[5] T. Minami, Y. Nishi, and T. Miyata, Appl. Phys. Express **6**, 044101 (2013).

[6] Y.S. Lee, D. Chua, R.E. Brandt, S.C. Siah, J. V Li, J.P. Mailoa, S.W. Lee, R.G. Gordon, and T. Buonassisi, Adv. Mater. **26**, 4704 (2014).

[7] T.G. Allen and A. Cuevas, Appl. Phys. Lett. **105**, 031601 (2014).

[8] M. Fleischer and H. Meixner, Sensors Actuators B Chem. **4**, 437 (1991).

[9] E. Nogales, J. a García, B. Méndez, J. Piqueras, K. Lorenz, and E. Alves, J. Phys. D. Appl. Phys. **41**, 065406 (2008).

[10] D.J. Comstock and J.W. Elam, Chem. Mater. **24**, 4011 (2012).

[11] K. Sasaki, A. Kuramata, T. Masui, E.G. Víllora, K. Shimamura, and S. Yamakoshi, Appl. Phys. Express **5**, 035502 (2012).

[12] B.K. Newman, E. Ertekin, J.T. Sullivan, M.T. Winkler, M. a. Marcus, S.C. Fakra, M.-J. Sher, E. Mazur, J.C. Grossman, and T. Buonassisi, J. Appl. Phys. **114**, 133507 (2013).

[13] S.C. Siah, R. Jaramillo, R. Chakraborty, P.T. Erslev, C. Sun, T. Weng, M.F. Toney, G. Teeter, and T. Buonassisi, IEEE J. Photovoltaics 1 (2014).

[14] S.C. Siah, S.W. Lee, Y.S. Lee, J. Heo, T. Shibata, C.U. Segre, R.G. Gordon, and T. Buonassisi, Appl. Phys. Lett. **104**, 242113 (2014).

[15] See supplemental material at [URL will be inserted by AIP] for full Sn *K*-edge XANES spectra.

[16] L. Qiao, H.Y. Xiao, S.M. Heald, M.E. Bowden, T. Varga, G.J. Exarhos, M.D. Biegalski, I.N. Ivanov, W.J. Weber, T.C. Droubay, and S.A. Chambers, J. Mater. Chem. C **1**, 4527 (2013).

[17] See supplemental material at [URL will be inserted by AIP] for XRD measurements for ALD and PLD thin films.

[18] D.C. Koningsberger and R. Prins, *X-Ray Absorption: Principles, Applications, Techniques of EXAFS, SEXAFS, and XANES* (Blackwell Scientific Publications, Eindhoven, The Netherlands, 1988).

[19] P. Villars, *Material Phases Data System (MPDS)* (CH-6354 Vitznau, Switzerland, 2014).

[20] S. Grindy, B. Meredig, S. Kirklin, J.E. Saal, and C. Wolverton, Phys. Rev. B **87**, 1 (2013).

[21] B. Ravel and M. Newville, J. Synchrotron Radiat. **12**, 537 (2005).

[22] T.C. Lovejoy, R. Chen, E.N. Yitamben, V. Shutthanadan, S.M. Heald, E.G. Villora, K. Shimamura, S. Zheng, S.T. Dunham, F.S. Ohuchi, and M. a. Olmstead, J. Appl. Phys. **111**, 123716 (2012).

[23] See supplemental material at [URL will be inserted by AIP] for Ga *K*-edge EXAFS parameters for all samples.

[24] See supplemental material at [URL will be inserted by AIP] for magnitude and real part of the fitted Fourier-transformed EXAFS spectra for (a) Ga and (b) Sn *K*-edges.

[25] See supplemental material at [URL will be inserted by AIP] for magnitude and imaginary part of the fitted Fourier-transformed EXAFS spectra for (a) Ga and (b) Sn *K*-edges..

[26] E.G. Víllora, S. Arjoca, K. Shimamura, D. Inomata, and K. Aoki, in *SPIE 8987, Oxide-Based Mater. Devices V, 89871U (March 8, 2014)* (2014).

[27] J.B. Varley, J.R. Weber, A. Janotti, and C.G. Van de Walle, Appl. Phys. Lett. **97**, 142106 (2010).

[28] M.B. Maccioni, F. Ricci, and V. Fiorentini, Appl. Phys. Express 021102 (2015).

[29] T.H. Yeom, I.G. Kim, S.H. Lee, S.H. Choh, and Y.M. Yu, J. Appl. Phys. **93**, 3315 (2003).

[30] I.G. Kim, T.H. Yeom, S.H. Lee, Y.M. Yu, H.W. Shin, and S.H. Choh, J. Appl. Phys. **89**, 4470 (2001).

[31] A. Zakutayev, N.H. Perry, T.O. Mason, D.S. Ginley, and S. Lany, Appl. Phys. Lett. **103**, 232106 (2013).

Captions:

Figure 1: Net carrier density of β-Ga_2O_3:Sn single crystals, ALD a-Ga_2O_3:Sn film and PLD a-Ga_2O_3:Sn film as a function of varying [Sn]. The deduced upper limit for a-Ga_2O_3:Sn films is indicated by the dashed line.

Figure 2: Sn edge XANES spectra for (a) SC β-Ga_2O_3:Sn, (b) PLD a-Ga_2O_3:Sn and (c) ALD a-Ga_2O_3:Sn samples. The dashed, dashed-dotted and dotted lines represent Sn(0) metal (dashed-line), Sn(II)O (dashed-dotted line) and Sn(IV)O_2 (dotted line) references respectively.

Figure 3: Fourier-transformed EXAFS spectra plotted as the magnitude, $|\chi(R)|$, for (a) Ga and (b) Sn *K*-edges. The dark and light grey regions represent the first and second shell fitting windows for the SC sample at the Sn *K*-edge. Note the poor fit for Sn on the Ga1 site for the SC sample.

Figure 4: k^2-weighted EXAFS spectra for (a) Ga and (b) Sn K-edges. Fits to both the Sn_{Ga1} and Sn_{Ga2} for the SC sample are shown in (b).

Table I: Sn *K*-edge EXAFS parameters for all samples. The SC is fitted by assuming either Sn substitution on Ga1 and Ga2 sites. The best fit is obtained for Sn substitution at Ga2 site. Scattering path-lengths up to 3.5 Å are considered for fitting the SC sample.

Figure S.1: Full Sn *K*-edges XANES spectra plotted for all samples.

Figure S.2: Wide angle XRD spectra for the ALD and PLD Ga_2O_3:Sn films. Data are plotted in Q, which is defined as $Q = [4\pi*\sin(\theta)]/\lambda$ or $Q = 2\pi/d$, where λ is X-ray wavelength and d is the d-spacing. Position of selected diffraction planes are also indicated by the vertical lines.

Figure S.3: Magnitude (thin solid line) and real part (thick solid line) of the fitted Fourier-transformed EXAFS spectra for (a) Ga and (b) Sn *K*-edges.

Figure S.4: Magnitude (thin solid line) and imaginary part (thick solid line) of the fitted Fourier-transformed EXAFS spectra for (a) Ga and (b) Sn *K*-edges.

Table S.I Ga *K*-edge EXAFS parameters for all samples. Scattering path-lengths up to 3.5 Å are considered for fitting the SC sample.

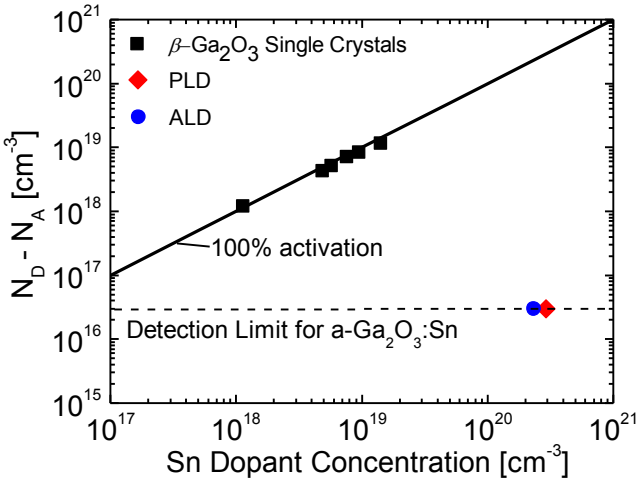

Figure 5: Net carrier density of β-Ga_2O_3:Sn single crystals, ALD a-Ga_2O_3:Sn film and PLD a-Ga_2O_3:Sn film as a function of varying [Sn]. The deduced upper limit for a-Ga_2O_3:Sn films is indicated by the dashed line.

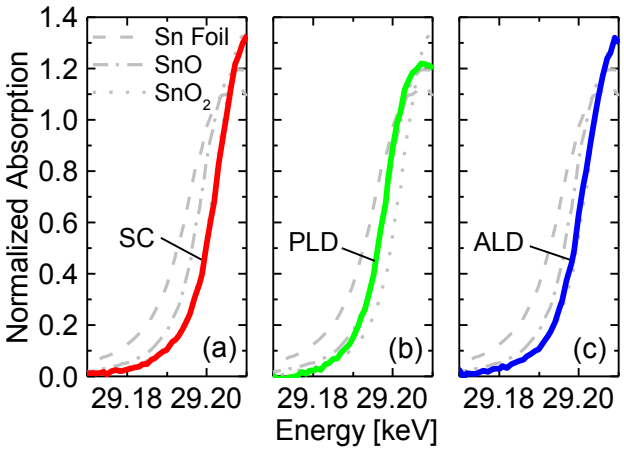

Figure 6: Sn edge XANES spectra for (a) SC β-Ga_2O_3:Sn, (b) PLD a-Ga_2O_3:Sn and (c) ALD a-Ga_2O_3:Sn samples. The dashed, dashed-dotted and dotted lines represent Sn(0) metal (dashed-line), Sn(II)O (dashed-dotted line) and Sn(IV)O_2 (dotted line) references respectively.

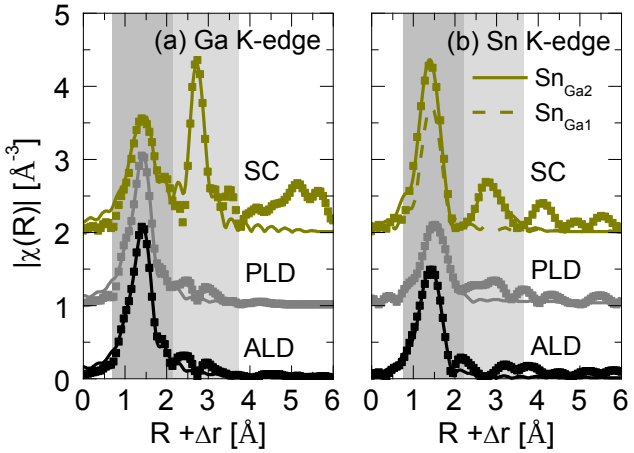

Figure 7: Fourier-transformed EXAFS spectra plotted as the magnitude, $|\chi(R)|$, for (a) Ga and (b) Sn *K*-edges. The dark and light grey regions represent the first and second shell fitting windows for the SC sample at the Sn *K*-edge. Note the poor fit for Sn on the Ga1 site for the SC sample.

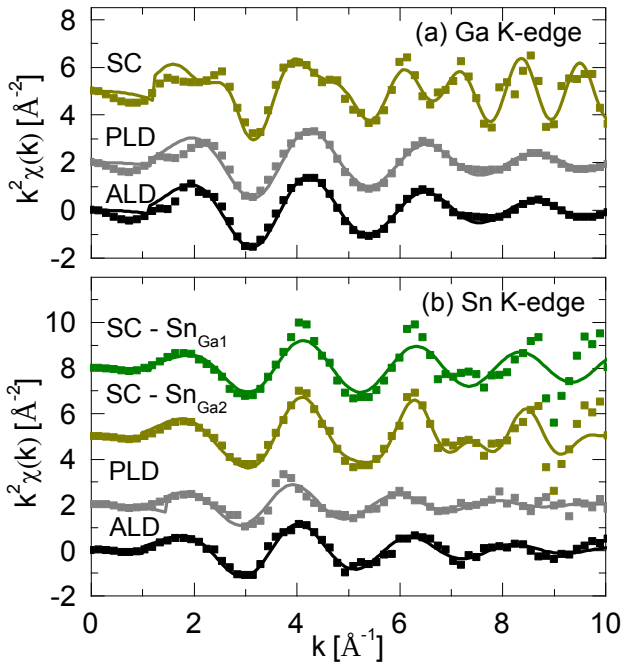

Figure 8: k^2-weighted EXAFS spectra for (a) Ga and (b) Sn K-edges. Fits to both the Sn_{Ga1} and Sn_{Ga2} for the SC sample are shown in (b).

Table II: Sn *K*-edge EXAFS parameters for all samples. The SC is fitted by assuming either Sn substitution on Ga1 and Ga2 sites. The best fit is obtained for Sn substitution at Ga2 site. Scattering path-lengths up to 3.5 Å are considered for fitting the SC sample.

	Site	Shell	Path Description	*N*	R_{eff} [Å]	ΔE_0 [eV]	σ^2 [Å^{-2}]	R-Factor
SC	Ga1	First	[Sn1] – O1,1 – [Sn1]	1	1.90(1)	5(2)	0.000(2)	0.05
			[Sn1] – O2,1 – [Sn1]	1	1.88(1)			
			[Sn1] – O3,1 – [Sn1]	2	1.84(1)			
	Ga2	First	[Sn2] – O1,1 – [Sn2]	2	1.959(3)	3.6(3)	0.0010(5)	0.01
			[Sn2] – O2,1 – [Sn2]	1	1.996(3)			
			[Sn2] – O2,2 – [Sn2]	2	2.062(3)			
			[Sn2] – O3,1 – [Sn2]	1	1.940(3)			
		Second	[Sn2] – Ga1,1 – [Sn2]	1	3.37(2)	3.6(3)	0.007(1)	
			[Sn2] – Ga1,2 – [Sn2]	2	3.42(2)			
			[Sn2] – Ga1,3 – [Sn2]	2	3.47(2)			
			[Sn2] – Ga1,4 – [Sn2]	2	3.55(2)			
			[Sn2] – Ga2,1 – [Sn2]	2	3.06(1)			
			[Sn2] – Ga2,2 – [Sn2]	2	3.09(1)			
			[Sn2] – O1,2 – [Sn2]	1	3.34(6)		0.02(1)	
			[Sn2] – O1,3 – [Sn2]	1	3.48(6)			
			[Sn2] – O2,3 – [Sn2]	2	3.63(6)			
			[Sn2] – O3,2 – [Sn2]	1	3.42(6)			
			[Sn2] – O3,3 – [Sn2]	1	3.34(6)			
			[Sn2] – O3,4 – [Sn2]	2	3.46(6)			
ALD		First	[Sn] – O3,1 – [Sn]	5.0(2)	2.030(3)	4.4(3)	0.0076(6)	0.005
PLD		First	[Sn] – O3,1 – [Sn]	5.1(2)	2.117(4)	8.2(3)	0.0128(8)	0.008

Supplemental Figures:

Dopant activation in Sn-doped Ga_2O_3 investigated by X-ray absorption spectroscopy

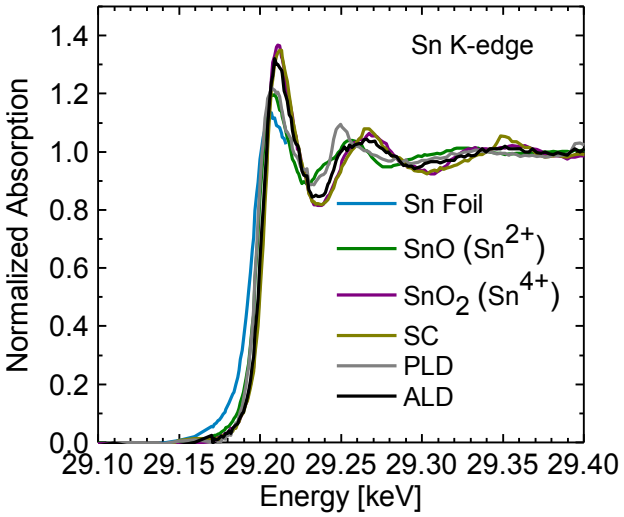

Figure S.1: Full Sn *K*-edges XANES spectra plotted for all samples.

Dopant activation in Sn-doped Ga_2O_3 investigated by X-ray absorption spectroscopy

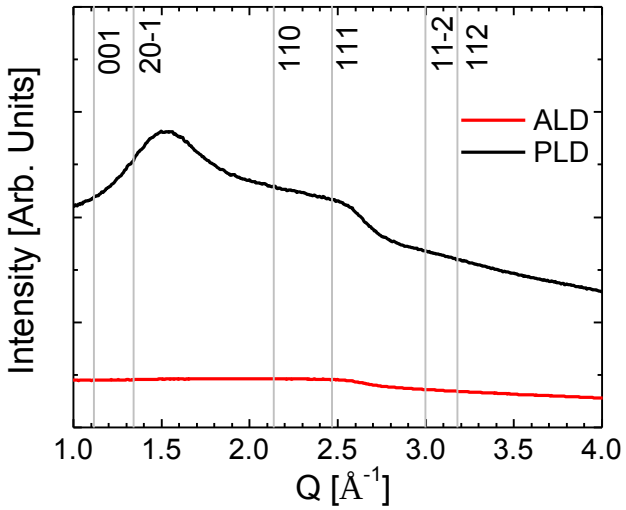

Figure S.2: Wide angle XRD spectra for the ALD and PLD Ga_2O_3:Sn films. Data are plotted in Q, which is defined as $Q = [4\pi*\sin(\theta)]/\lambda$ or $Q = 2\pi/d$, where λ is X-ray wavelength and d is the d-spacing. Position of selected diffraction planes are also indicated by the vertical lines.

Dopant activation in Sn-doped Ga_2O_3 investigated by X-ray absorption spectroscopy

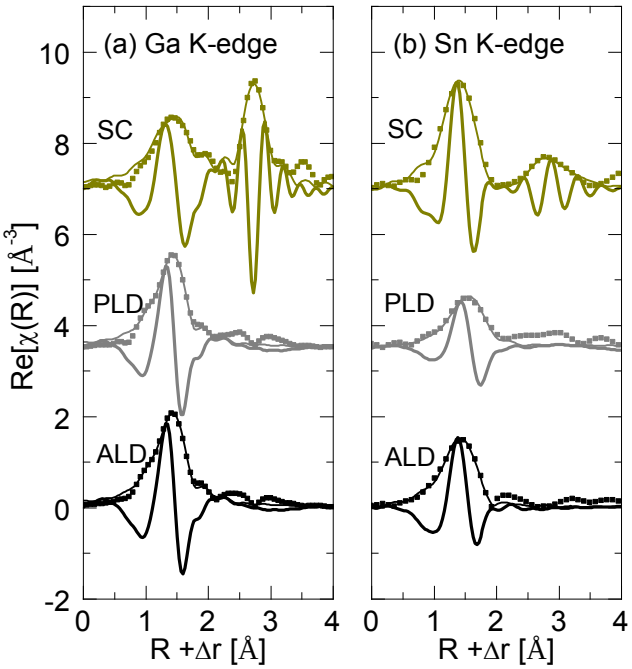

Figure S.3: Magnitude (thin solid line) and real part (thick solid line) of the fitted Fourier-transformed EXAFS spectra for (a) Ga and (b) Sn *K*-edges.

Dopant activation in Sn-doped Ga_2O_3 investigated by X-ray absorption spectroscopy

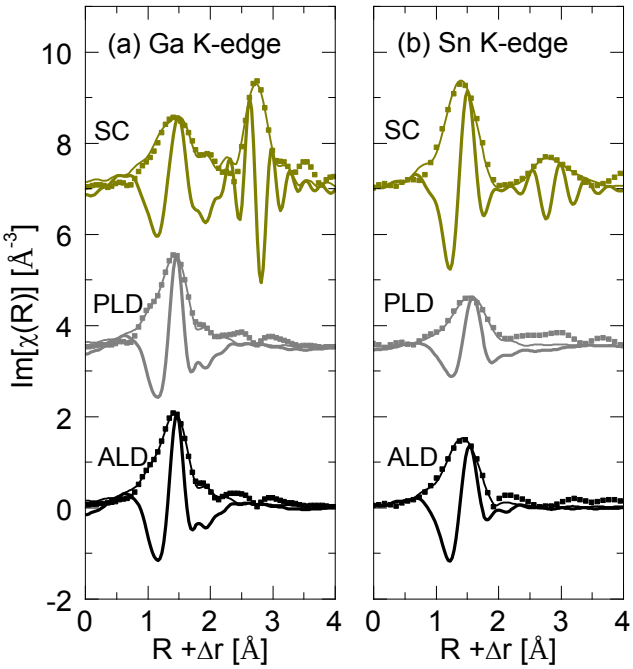

Figure S.4: Magnitude (thin solid line) and imaginary part (thick solid line) of the fitted Fourier-transformed EXAFS spectra for (a) Ga and (b) Sn *K*-edges.

Table S.I Ga *K*-edge EXAFS parameters for all samples. Scattering path-lengths up to 3.5 Å are considered for fitting the SC sample.

	Site	Shell	Path Description	*N*	R_{eff} [Å]	ΔE_0 [eV]	σ^2 [Å^{-2}]	R-Factor
SC	Ga1	First	[Ga1] – O1,1 – [Ga1]	1	1.85(2)	5.7(5)	0.008(1)	0.03
			[Ga1] – O2,1 – [Ga1]	1	1.88(2)			
			[Ga1] – O3,1 – [Ga1]	2	1.84(2)			
		Second	[Ga1] – Ga1,1 – [Ga1]	2	3.04(2)	-10.3(8)	0.0001(1)	
			[Ga1] – Ga2,1 – [Ga1]	1	3.264(4)			
			[Ga1] – Ga2,2 – [Ga1]	2	3.307(4)			
			[Ga1] – Ga2,3 – [Ga1]	2	3.346(4)			
			[Ga1] – Ga2,4 – [Ga1]	2	3.443(4)			
			[Ga1] – O1,2 – [Ga1]	2	3.24(4)	5.7(5)	0.0001(1)	
			[Ga1] – O1,3 – [Ga1]	1	3.33(4)			
			[Ga1] – O1,4 – [Ga1]	2	3.55(4)			
			[Ga1] – O2,2 – [Ga1]	1	3.39(8)			
			[Ga1] – O3,2 – [Ga1]	2	3.42(2)			
			[Ga1] – O3,3 – [Ga1]	2	3.49(2)			
	Ga2	First	[Ga2] – O1,1 – [Ga2]	2	1.95(2)	5.7(5)	0.008(1)	
			[Ga2] – O2,1 – [Ga2]	1	2.00(2)			
			[Ga2] – O2,2 – [Ga2]	2	2.05(2)			
			[Ga2] – O3,1 – [Ga2]	1	1.94(2)			
		Second	[Ga2] – Ga1,1 – [Ga2]	1	3.27(2)	-10.3(8)	0.0001(1)	
			[Ga2] – Ga1,2 – [Ga2]	2	3.31(2)			
			[Ga2] – Ga1,3 – [Ga2]	2	3.35(2)			
			[Ga2] – Ga1,4 – [Ga2]	2	3.44(2)			
			[Ga2] – Ga2,1 – [Ga2]	2	3.037(4)			
			[Ga2] – Ga2,2 – [Ga2]	2	3.071(4)			
			[Ga2] – O1,2 – [Ga2]	1	3.48(4)	5.7(5)	0.0001(1)	
			[Ga2] – O1,3 – [Ga2]	1	3.62(4)			
			[Ga2] – O2,3 – [Ga2]	2	3.63(8)			
			[Ga2] – O3,2 – [Ga2]	1	3.42(2)			
			[Ga2] – O3,3 – [Ga2]	1	3.47(2)			
			[Ga2] – O3,4 – [Ga2]	2	3.60(2)			
ALD	-	First	[Ga] – O3,1 – [Ga]	4.2(1)	0.037(2)	5.0(2)	0.0059(3)	0.003
PLD	-	First	[Ga] – O3,1 – [Ga]	3.9(1)	0.032(3)	5.3(3)	0.0051(5)	0.006